Frequency domain model for railway wheel squeal resulting from unsteady longitudinal creepage

D.J. Fourie[1, 2], P.J. Gräbe[1], P.S. Heyns[3] and R.D. Fröhling[2]

[1] Chair in Railway Engineering, University of Pretoria, South Africa

[2] Transnet Freight Rail

Room 420, NZASM Building, 6 Minnaar Street, Pretoria, South Africa, 0001

Tel: +27 12 315 2203, Fax: +27 12 315 3096, E-mail: danie.fourie4@transnet.net

[3] Department of Mechanical and Aeronautical Engineering, University of Pretoria, South Africa

Abstract

Railway wheel squeal is an unresolved noise pandemic facing the railway industry. Wheel squeal results from frictional self-excited vibration occurring in the wheel-rail contact. Solving the problem of squeal requires researchers to work towards a squeal model that can predict squeal wholly and in every situation. This will allow for squeal to be resolved during the design stages. The current research presents a frequency domain model for the excitation of squeal due to longitudinal creepage with rising, constant and falling friction. In this model the time varying part of the longitudinal creep force is modelled as a feedback loop and tested for stability with the Nyquist criterion. Crucial to the instability is modelling the dynamics of a wheel taking into consideration the moving load nature of the rotating wheel. If wheel rotation is accounted for in the model, modes in a doublet can become unstable through mode-coupling in the presence of large longitudinal creepage. The results of the model provide good agreement with that of squeal occurring on-track. Positive flow of energy for the modelled case of squeal results from the dynamic friction and normal forces being in phase with one another as well as the friction force causing normal displacement at the wheel-rail contact that is in phase with the normal displacement that caused the normal force in the first place. This closed phase loop causes positive interference of the normal vibration in the wheel-rail contact and allows the vibration amplitude to grow. Extending the model to include lateral creepage shows that the vibration of the wheel-rail contact can be unstable due to unsteady longitudinal creepage for more directions of the resulting creep force compared to unsteady lateral creepage in a case with constant friction.

1 Introduction

Railway wheel squeal is an intense tonal noise that may arise when railway vehicles steer with large creep forces in the wheel-rail contact. In spite of all the progress made over the past four decades, many researchers think of squeal as chaotic rather than deterministic. This is because squeal often does not occur consistently for seemingly similar conditions, and the varying success of known treatments in eliminating squeal under different circumstances. It may also be that squeal appears to be chaotic as all the parameters influencing squeal are simply not yet fully understood. Currently researchers studying squeal are working towards a squeal model that can predict squeal comprehensively. One of the big debates is the relevance of falling friction and mode-coupling to the development of squeal in practice.

Lateral creepage is the dominant source of instability for squeal and most models in the literature account specifically for squeal due to unsteady lateral creepage [1-14]. Models for unsteady lateral creepage can be further divided into negative friction models [1-9] and constant friction models, modelling mode-coupling instability [10-14].

Although previously disregarded, increasing evidence suggests the importance of flange contact and longitudinal creepage as sources of instability for squeal.

Two theories exist in the literature about the relationship between flange contact and squeal. The first states that flange contact alone will not produce squeal and that flange contact, with the flange rubbing on the gauge face,

reduces the likelihood of stick-slip due to lateral slip and the levels of squeal noise at wheels in flange contact [15]. The second theory acknowledges that flange contact can produce tonal squeal, although the mechanisms governing squeal in such conditions are not yet fully understood [16-17]. It is however known that gauge face lubrication eliminates tonal squeal at sites where squeal originate from the leading outer wheel of a bogie. In a recent study Zenzerovic [18] showed that modelling two-point wheel-rail contact can actually be important to capture squealing of curve-outer wheels, although the model was not validated against experimental results at the time. In [18] squeal is a result of the dynamic interplay of the two contact points and the presence of two closely spaced wheel modes, similar to model of Squicciarini et al. [19] that modelled flange-back contact squeal and validated against on-track measurements.

Concerning longitudinal creepage, Huang et al. [9] use a negative friction model to demonstrate that the trailing wheels in a tight curve subject to large longitudinal creepage and small lateral creepage is unstable in the fundamental circumferential mode. Because the fundamental circumferential mode generally occurs between 50 and 100 Hz [20], longitudinal creepage is not considered relevant to squeal. Instead longitudinal creepage is considered relevant to corrugation formation. In contrast to the above, Fourie et al. [21] have shown that the wheels underneath some heavy haul trains on a 1000 m curve squeal in the presence of large longitudinal creepage and little lateral creepage at frequencies between 3.5 and 6 kHz. Vehicle dynamics simulations have shown that the combination of worn wheel and rail profiles cause affected Scheffel self-steering bogies [22] under empty CR13/14 Iron Ore wagons to over-steer in the test curve [23]. Over-steering causes both wheelsets of the bogie to displace laterally towards the outside of the curve causing high levels of longitudinal creepage.

To address the disconnect between the current literature that does not consider unsteady longitudinal creepage as a mechanism for squeal and the experimental evidence in [21] that strongly suggests the opposite, the current research tests the following hypothesis: The forward and/or backward travelling waves gives rise to mode-coupling type instability in the presence of wheel rotation. This hypothesis follows from the following argument:

Hoffmann et al. [24] illustrate mode-coupling instability using a simple two degree of freedom model. They demonstrate how energy can be transferred from the frictional system to vibrational energy as a consequence of simultaneous out-of-phase oscillations of the friction force and displacement tangential to the friction force. The above phase relationship for cyclic energy transfer is realised when out-of-phase tangential and normal displacements are present at the frictional interface. For positive energy transfer the tangential oscillation must lag behind the normal oscillation and for negative energy transfer the normal oscillation must lag behind the tangential oscillation. The maximum positive energy transfer is realised when the tangential oscillation lags 90° behind the normal oscillation.

Considering longitudinal creepage in the wheel-rail contact the above phase relationship between tangential and normal oscillations for positive energy transfer is realised for doublet modes as a consequence of the moving load nature of the rotating wheel. This follows from [25] that show how the independent sine and cosine doublet modes without cross-coupling for a stationary wheel become two complex modes with radial/longitudinal cross-coupling (90° phase relationship) with respect to the contact when the moving load nature of the wheel is considered. To understand if the forward and/or backward travelling waves can give rise to mode-coupling instability the current research combines an existing model for wheel squeal based on the Nyquist criterion [5-7] with a model for the moving load nature of the rotating wheel [25] in the presence of large longitudinal creepage. This approach of including the moving load nature of the rotating wheel into a squeal model for unsteady longitudinal creepage has not been considered before. To date the effects of a rotating wheel has only been considered in a squeal model due to unsteady lateral creepage assuming constant friction and ignoring the effects of longitudinal creepage [26]. Pieringer et al. [26] shows that a non-rotating, sliding wheel is sufficient to capture the tendency to squeal although the rotation of the wheel delays the build-up of the stick-slip oscillation. A non-rotating wheel is sufficient to predict squeal due to unsteady lateral creepage as the cross-coupling between the radial and lateral degrees-of-freedom in the wheel-rail contact is similar for a stationary and rotating wheel [25].

In addition to the current research, the authors previously presented a frequency domain model for wheel squeal assuming a non-rotating sliding wheel in contact with the rail [27]. Although this model could accurately predict the experimentally measured squeal frequencies, instability only occurred for a coefficient of friction exceeding

12. Because of this unfeasibly high coefficient of friction, the model based on a non-rotating sliding wheel will not be considered further by the authors.

The structure of the current paper is as follows:

Firstly the wheel dynamics of a rotating wheel subject to a moving load is discussed. Hereafter the creep force-creepage relationship that will be used in the squeal model is presented. In an attempt to model curve squeal, authors assume different creep force-creepage models. As an example Périard [3], Huang et al. [9] and Squicciarini et al. [19] implemented a falling friction law in FASTSIM. FASTSIM is the name given by Kalker [28] for his simplified steady-state non-linear rolling contact theory. FASTSIM was born out of Kalker's efforts to reduce the computational cost associated with his "exact" rolling contact theory CONTACT [29] which today is the only available rolling contact theory that is fully non-linear and transient. Pieringer [12] implemented Kalker's theory CONTACT in her time-domain squeal model with a constant friction coefficient in addition to considering the roughness of the wheel and rail running surfaces. In their work De Beer et al. [5, 6] implement Vermeulen and Johnson's [30] approximate non-linear rolling contact theory with Kraft's [31] model for falling friction. Kraft's model for falling friction was also used by Fingberg [2]. On the other hand Huang et al. introduced a falling friction coefficient based on previous experimental roller-rig findings which were also used by Ding et al. [32]. In [18], Zenzerovic aims at making Pieringer's [12] squeal model faster by including a point contact model for the tangential contact defined beforehand using CONTACT.

Next the squeal model based on the Nyquist criterion is discussed as well as the wheel and rail models used in combination with the squeal model. This is followed by a discussion of the results of the model and a qualitative comparison with experimental measurements. Section 6 discusses a physical interpretation of the energy transfer mechanism responsible for squeal, whilst the last section of the paper extends the squeal model to include lateral creepage.

2 Wheel dynamics

The modes of vibration of the wheel are classified according to their predominant motion. This includes axial, radial and circumferential modes, having n nodal diameters and m nodal circles [33]. Axial modes are denoted (n,m). Radial and circumferential modes with more than 0 nodal circles do not occur in the frequency range of interest. These modes will be denoted (n,R) and (n,C).

In the wheel-rail system, the rotating/sliding wheel couples with a stationary rail. For a stationary wheel in contact with a rail, each sine and cosine doublet mode pair consists of two independent modes of the wheel without coupling in the contact area. This is because the anti-nodes of the one doublet mode become the nodes of the other doublet mode and vice versa.

Thompson [25] derived the dynamics of a rotating wheel due to the moving load nature of the wheel contact, ignoring gyroscopic effects and centrifugal stiffening. With the rotating wheel being exposed to moving loads, the doublet mode pairs become two complex modes which are rotating in opposite directions, and at frequencies of $\omega_{mn} \pm n\Omega$ (for $n > 0$). The deformation vector of both these travelling waves are given by $\Psi_{mn} = \Psi_{mn}^{I} + \mathrm{i}\Psi_{mn}^{II}$ in which I represents axial and radial displacements and rotation about the circumferential axis and II represents circumferential displacement and rotations about the radial and axial axes. Because a forward and backward travelling wave exists, the contact point mobility will have two resonance peaks for each natural frequency of the stationary wheel (ω_{mn}).

From [33], the vertical and longitudinal point mobility of the rotating wheel subject to moving load excitation as seen at the contact patch can be calculated using Eqs. (1) and (2) respectively

$$Y_{w,33}(\omega) = \mathrm{i}\omega \sum_{m,n} \left\{ \frac{\psi_{mn3}\psi_{mn3}}{2m_{mn}} \left(\frac{1}{d_{+}(\omega)} + \frac{1}{d_{-}(\omega)} \right) \right\} \tag{1}$$

$$Y_{w,11}(\omega) = \mathrm{i}\omega \sum_{m,n} \left\{ \frac{\psi_{mn1}\psi_{mn1}}{2m_{mn}} \left(\frac{1}{d_+(\omega)} + \frac{1}{d_-(\omega)} \right) \right\} \quad (2)$$

and the vertical/longitudinal cross mobility using Eq. (3).

$$Y_{w,31}(\omega) = \mathrm{i}\omega \sum_{m,n} \left\{ \frac{\psi_{mn1}\psi_{mn3}}{2m_{mn}} \left(\frac{-\mathrm{i}}{d_+(\omega)} + \frac{\mathrm{i}}{d_-(\omega)} \right) \right\} \quad (3)$$

Here ψ is the modeshape amplitude of mode (m, n), m_{mn} is the modal mass of the corresponding mode and $d_\pm$ is given by :

$$d_\pm = \omega_{mn}^2 - (\omega \pm n\Omega)^2 + 2\mathrm{i}\zeta_{mn}(\omega \pm n\Omega)\omega_{mn} \quad (4)$$

where ω_{mn} is the natural frequency and ζ_{mn} is the modal damping ratio.

The terms $Y_{w,31}$and $Y_{w,13}$ are skew-symmetric i.e. $Y_{w,31} = -Y_{w,13}$.

3 Creep force - Creepage relationships

Wheel-rail contact is made over a small contact patch. This small contact patch is responsible for reacting the normal load and transmitting the tangential forces that are necessary for traction, braking and vehicle guidance. The tangential force is transmitted between the wheel and rail through the simultaneous action of both adhesion and slip of the wheel and rail over the contact patch. As the slip between the wheel and the rail increases the adhesion coefficient approaches the Coulomb limit and gross sliding occurs in the contact when the contact patch is saturated with slip.

A creep force-creepage relationship describes the relationship between the tangential forces transmitted by the contact patch and the relative sliding velocity between the wheel and rail. This relative sliding velocity normalized by the rolling velocity of the wheel is denoted creepage.

Typical shapes of the creep force-creepage relationship for large longitudinal creep under dry and wet conditions according to [34] are shown in Figure 1.

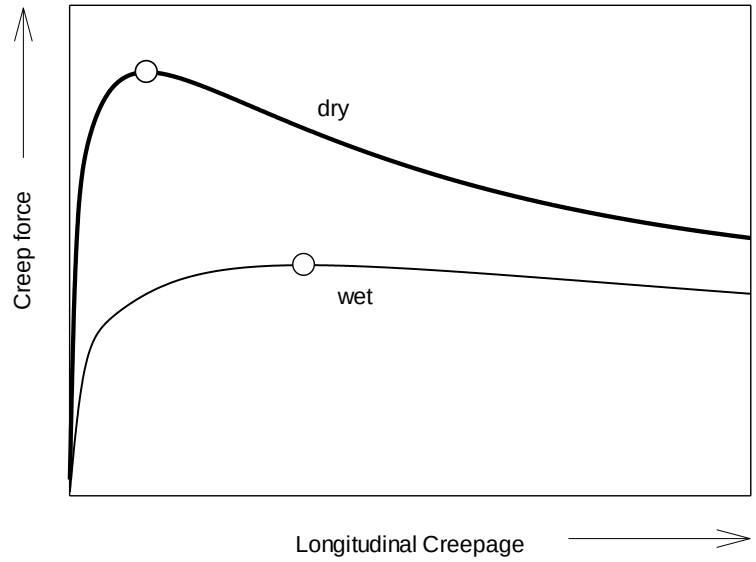

Figure 1. Typical shape of measured creep force-creepage functions for longitudinal creepage showing point of maximum adhesion (circle) for wet and dry conditions.

Evident from Figure 1, is an initial linear slope of the curve for small creepages. This linear slope then transitions to a non-linear region with a significantly reduced slope that reaches a point of maximum adhesion. At the point of maximum adhesion gross sliding occurs in the contact beyond which typically the relationship has a negative slope implying decreasing friction with increasing relative velocity. It is generally this negative slope of the friction curve beyond creep saturation that is identified as the source of instability for railway wheel squeal. This negative slope of the friction curve is equivalent to negative damping. This is however not the only mechanism of excitation for squeal as coupling between the tangential and normal dynamics of the wheel can also lead to instability in the presence of large creepages. Using a detailed high-frequency wheel-rail interaction model formulated in the time-domain and considering lateral creepage, Pieringer [12] shows that for a specific squeal case that develops at 5235 Hz the lateral contact force stays below the traction limit at all times. Squeal in this specific case was associated with the coupling of the (7,0) and (2,C) modes of the modelled wheel. This suggests that creep saturation is not a necessary prerequisite for squeal due to mode-coupling where the squeal results from coupling between the vertical and tangential dynamics of the wheel. As stated in the introduction Pieringer used CONTACT in her time-domain squeal model.

Kalker's non-linear rolling contact theories CONTACT and FASTSIM describe the case for scrupulously clean and smooth surfaces. In reality the surfaces are neither smooth nor clean and surface roughness as well as contamination at the wheel-rail interface have a remarkable impact on the initial slope of the creep force-creepage relationships that are measured during experiments [35]. In order to accommodate the effects of contamination and surface roughness a coefficient called "percent" Kalker is often introduced for accommodation of the initial slope of the creep force-creepage relationship (see e.g. [36]). Polach [34] introduced two reduction factors, one for the adhesion area (k_A) and the other for the slip area (k_S) to accommodate both the initial gradient and the gradient of the creep force-creepage function for large creep near creep saturation, as is typically measured for longitudinal creepage during locomotive adhesion. The gradient of the creep force-creepage function for low creepages corresponds to the reduction of Kalker's coefficient by

$$k = \frac{k_A + k_S}{2} \qquad k_A,\ k_S \leq 1 \tag{5}$$

In addition, Polach's model also considers falling friction that is typically measured for large creepage values by using a variable coefficient of friction expressed by

$$\mu = \mu_0[(1-A)e^{-Bv} + A] \tag{6}$$

where A is the ratio of limit friction coefficient μ_∞ at infinite slip velocity to maximum friction coefficient μ_0, v the creep velocity and B is the coefficient of exponential friction decrease.

In Polach's model, the adhesion coefficient for pure longitudinal creepage μ_1 is given by

$$\mu_1 = \frac{2\mu}{\pi}\left(\frac{k_A\varepsilon_1}{1+(k_A\varepsilon_1)^2} + \arctan(k_S\varepsilon_1)\right) \tag{7}$$

where ε_1 is the gradient of the tangential stress in the contact longitudinal direction given by

$$\varepsilon_1 = \frac{1}{4}\frac{G\pi ab C_{11}}{Q\mu}\lambda_1 \tag{8}$$

G is the shear modulus, a and b the contact area half axes of the assumed elliptical contact area in the longitudinal and transverse directions, Q the wheel load, λ_1 the longitudinal creepage and $C_{11}$the coefficient from Kalker's linear theory [29].

3.1 Creep – Creepage model assumed for current study

In practice the exact shape of the creep force-creepage relationship is seldom known, except in cases where this is explicitly measured during locomotive traction.

To define a creep force-creepage relationship for the current study, Polach's model using Eqs. (7) and (8) is used. To use Polach's model the following parameters need to be defined: the reduction variables k_A and k_S, the contact variables a, b, Q and C_{11} as well as the friction model μ.

Typically the reduction factor k for dry rails as evaluated from measurements is 0.6 to 0.85 [34]. Choosing the value of k as 0.85, due to the very little environmental contamination expected, and choosing a reduction factor for the area of adhesion k_A as 1.00, k_S is calculated using Eq. (5) as 0.70. Very little environmental contamination is expected based on the very high top-of-rail coefficient of friction of 0.64 measured in the test curve for dry wheel-rail contact conditions. The coefficient of friction was evaluated using a hand pushed tribometer in the test curve [23, 27].

Typical contact parameters for the wheel-rail contact area of a squealing wheel are available from the vehicle dynamics simulations reported in [23] and summarised in Table 1.

Table 1. Contact parameters from vehicle dynamics simulation

Contact parameter	Value	Unit
a	4.5	mm
b	2.5	mm
Q	20	kN
C_{11}	5.31	-

Not knowing the parameters A and B from experimental measurements to define a falling friction model according to Eq. (6), Kraft's [31] model for falling friction (as was used in previous squeal models) is used.

Kraft's formula for the friction coefficient, derived theoretically but adapted to fit experimental measurements due to longitudinal creepage, can be written as

$$\mu = \mu_0\left[1 - 0.5\mathrm{e}^{-0.138/|v|} - 0.5\mathrm{e}^{-6.9/|v|}\right] \quad (9)$$

where v is the sliding velocity which can be expressed as $v = \lambda V_0$. Here λ is the creepage and V_0 the rolling velocity. For the present study, μ_0 is chosen as 0.64 as measured for dry wheel-rail contact conditions using a hand pushed tribometer in the test curve.

The creep force-creepage relationship assumed in the current study and calculated for a speed of 60 km/h (typical of the speed in the 1000 m test curve for the squealing iron ore wagons) with the above defined parameters is shown in Figure 2. The adhesion optimum occurs at 0.62 % longitudinal creepage, beyond which the friction curve has a negative slope.

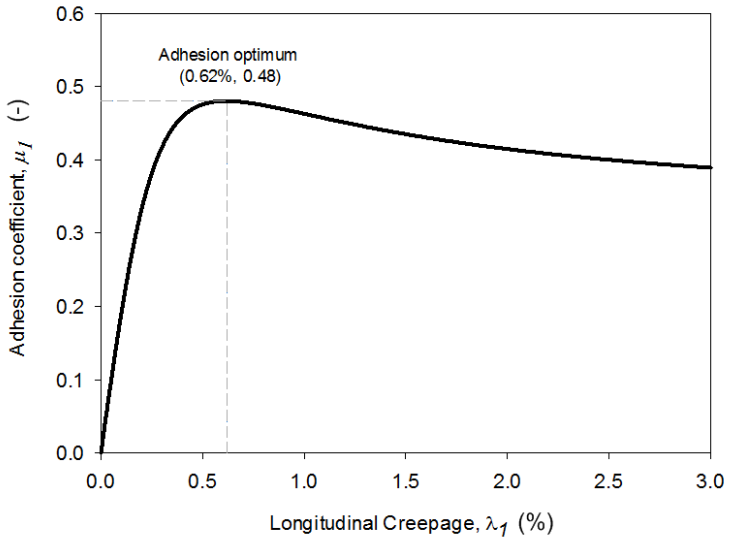

Figure 2. Adhesion curve assumed for current study

The operating point of the squealing wheel on the adhesion curve is crucial to the instability. It is known a priori that creep saturation with a negative slope of the adhesion curve is a pre-requisite for squeal to occur due to falling friction. This is because a negative gradient of the adhesion curve indicates negative frictional damping. On the other hand a positive gradient of the adhesion curve corresponds to positive frictional damping. Judging from the shape of the adhesion curve in Figure 2 and knowing that creep saturation is not a necessary pre-requisite for squeal due to mode-coupling [12] it can be postulated that the significantly reduced gradient of the adhesion curve leading up to the adhesion optimum might not provide enough positive damping to overcome the positive energy transfer associated with mode-coupling instability and hence instability can occur even for a positive gradient of the creep force-creepage relationship in the case of mode-coupling instability.

It is then also the case that the 0.57 % longitudinal creepage predicted by the vehicle dynamics simulations for the investigated squealing case [23] most likely places the squealing wheel at a point on the adhesion curve before creep saturation occurs. The 0.57 % longitudinal creepage calculated in the multi body dynamics simulation presented in [23] corresponds to a rolling radius difference, Δr, between the left and right wheels of 4.8 mm. The dynamic creepage value of 0.57 % calculated by the multi body dynamics simulation takes into consideration material deformation in the contact area in addition to the kinematic rolling of the wheelset. Only considering the kinematic rolling of the wheelset, a rolling radius difference of 4.8 mm yields a longitudinal creepage of 0.93 %. It can thus be seen that assuming the kinematic formulation for longitudinal creepage, i.e

$\lambda_1 = {}^{\Delta r}/_{r_0}$ where r_0 is the mean rolling radius between the left and right wheels, significantly overpredicts the longitudinal creepage because material deformation is not considered in the contact area. In [21] the authors assumed the kinematic formulation for longitudinal creepage when they estimated the longitudinal creepage in the wheel-rail contact for the squealing wheels in the test curve based on measured wheel and rail profiles and measured wheelset lateral displacements. By comparing the dynamic longitudinal creepage calculated in the vehicle dynamics simulation with the kinematic creepage estimate, it becomes clear that the kinematic formulation as used in [21] significantly overpredicts the creepage because material deformation is not considered in the contact area.

4 Modelling of wheel squeal

Squeal models combine wheel dynamics, rail/track dynamics and contact dynamics into a squeal model that can solve wheel-rail interaction at high frequencies in either the frequency or time domains. The friction law (negative or constant friction) is contained in the contact model. Presently researchers studying wheel squeal realise the importance of both falling and constant friction in the excitation of squeal although it is not yet clear to what extent each contributes to the development of squeal in practice [32, 37-38].

Frequency domain models describe the instability of the linearised system, determining which wheel modes are prone to squeal. Not all modes with negative damping in the simulation results will be found in experimental squeal results. This is because the linear stability analysis only indicates the tendency to squeal and not which mode(s) will eventually grow into limit cycles [39]. On the other hand, time domain models can include all non-linearities and transient effects in the wheel-rail contact and can determine true squeal amplitudes and frequencies, but at the expense of computational resources and time. In this paper a linear frequency domain method is used to study squeal as a first insight into the squeal phenomenon resulting from unsteady longitudinal creepage.

Two frequency domain methods are widely used to study railway wheel squeal instability, through complex eigenvalue analysis and the Nyquist criterion [37].

Complex eigenvalue analysis calculates the eigenvalues of the contact coupled wheel-rail system and instability is identified when the real part of at least one eigenvalue becomes positive. The positive real part of the eigenvalue is equivalent to negative damping, feeding energy into the vibration. In relation to railway wheel squeal this approach was first considered by Chen et al. [10] and later by Pieringer et al. [13], Wang et al. [14] as well as by Fourie et al. [27].

The Nyquist criterion can be used to test a system for stability if it can be represented by a control system with a feedback loop. The system is unstable for frequencies where the Nyquist contour $H(\omega)$ passes the real axis at the right side of (+1,0) on the Nyquist (real vs. imaginary) plane [5]. This corresponds to a loop gain larger than one.

4.1 Frequency domain model using the Nyquist criterion

The self-excited vibration between the wheel-rail contact forces and their responses can be described as a feedback loop. Combining the equations for contact dynamics, wheel dynamics and rail dynamics, produces a loop gain for the tangential contact force. If the loop gain encircles the point (+1,0) on the Nyquist plane, the system is unstable. By plotting the real part of the open loop transfer function against frequency, the frequencies associated with these unstable points can be defined as potential unstable frequencies.

Such a frequency domain model to describe squeal due to unsteady lateral creepage using a feedback loop was developed by De Beer et al. [5, 6]. Whilst De Beer et al. include the variation of the normal contact force in their frequency domain squeal model the motivation behind it was not to study mode-coupling instability. Instead the variation in the normal force was included to account for the influence that the lateral contact position on the wheel tread has on squeal noise due to lateral creepage with a negative friction characteristic.

Thompson and Monk-Steel [7] extended the model developed by De Beer et al. to include longitudinal and spin creepage in addition to lateral creepage and normal load variations.

From [7], for a case where only longitudinal creepage is important in producing squeal the loop gain for the potentially unstable longitudinal creep force f_1 is given by

$$-\left(Y_{11}-\frac{Y_{13}Y_{31}}{Y_{33}}\right)\left(\frac{F_3}{V}\frac{\partial\mu_1}{\partial\lambda_1}\right)-\left(\mu_1+\frac{F_3}{V}\frac{\partial\mu_1}{\partial f_3}\right)\frac{Y_{31}}{Y_{33}} \tag{10}$$

where the indices 1 and 3 describe the longitudinal and normal directions with respect to the contact patch and described in Figure 3. $Y_{ij}=Y_{w,ij}+Y_{r,ij}+Y_{c,ij}$ is the sum of the wheel ($Y_{w,ij}$), track ($Y_{r,ij}$) and contact spring ($Y_{c,ij}$) mobilities. Mobility refers to the ratio of the output velocity to a harmonically varying unit input force at a given frequency. F_3 is the quasi-static vertical contact force and V the rolling velocity of the wheel. $\mu_1$is the adhesion coefficient in the longitudinal direction, $\partial\mu_1/\partial\lambda_1$ is the gradient of the creep force-creepage function for longitudinal creepage whilst $\partial\mu_1/\partial f_3$ is the dependence of the adhesion coefficient on the normal force. The term $\partial\mu_1/\partial f_3$ is only relevant in the unsaturated regime where there is still an adhesion zone in the contact. This term reduces to zero for creep saturation. The term $\partial\mu_1/\partial f_3$ is ignored in the current model and Eq. (10) simplifies to

$$-\left(Y_{11}-\frac{Y_{13}Y_{31}}{Y_{33}}\right)\left(\frac{F_3}{V}\frac{\partial\mu_1}{\partial\lambda_1}\right)-(\mu_1)\frac{Y_{31}}{Y_{33}} \tag{11}$$

The first term of Eq. (11) represents the excitation due to falling friction, whereas the second term represents the influence of variations in the normal force on the lateral force. For a positive relationship of the creep force-creepage relationship, the first term can also represent positive frictional damping.

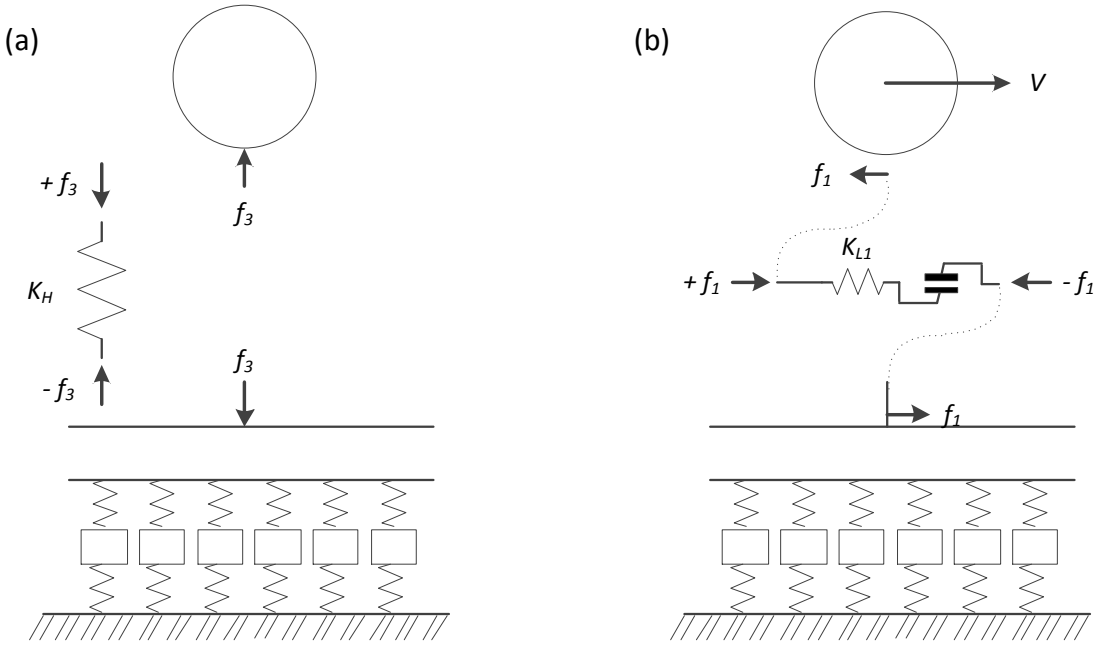

Figure 3. Sign conventions at wheel-rail interface: (a) Normal/Vertical direction, (b) Longitudinal direction

4.2 Wheel model

Modal parameters of the stationary wheel are calculated from a finite element (FE) model. The equivalent modal parameters of the rotating wheel (which is excited and observed in a fixed contact point) are expressed as a function of the rotational speed and the original stationary status modal parameters using Eqs. (1) to (3).

The wheel considered in the FE model is a 916 mm freight wheel, corresponding to wheel type A in [21]. A 3D model of the wheel was developed. This was done by constructing a 2D mesh of a single cross section of the wheel (see Figure 4) which was then revolved 100 times around the circumference using an angular spacing of 3.6° to create 3D brick elements. With eight being the largest number of nodal diameters for any mode in the frequency range between 0 and 6 kHz, a circumferential division of 100 elements exceeds the minimum recommended number of elements of six per structural wavelength [33] in the circumferential wheel direction. Only a single wheel of the railway wheelset was modelled, with the axle omitted and the wheel rigidly constrained at the center of the hub. The omission of the axle results in negligible errors for mode shapes with two or more nodal diameters [33]. In total the model consisted of 98 041 nodes and 287 049 degrees of freedom and was evaluated between 0 and 6 kHz. Example mode shapes calculated with the 3D model of the wheel are shown in Figures 5(a) to (c). The finite elements of the mode shapes in the contact plane (on the right side of each mode in Figure 5) have been coloured dark grey from the wheel hub to the wheel tread to assist with visualising the behaviour of the mode shape in the wheel-rail contact.

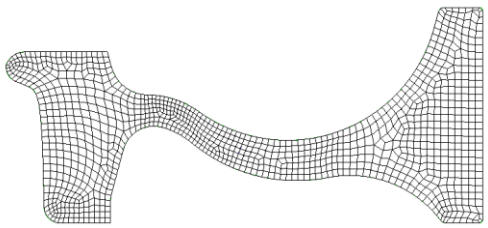

Figure 4. 2D mesh of wheel that was revolved to obtain 3D model of wheel

Figure 5. Example mode shapes of the 3D wheel model: (a) (2,0) cosine doublet (b) (2,C) cosine doublet (c) (7,R) cosine doublet

The wheel material properties used in the model is a Modulus of Elasticity of 210 GPa, a Poisson's ratio of 0.3 and a density of 7850 kg/m^3. The eigenfrequencies of all modes with two and more nodal diameters were updated to reflect the experimentally measured damping ratios according to Table 2. Eigenmodes with zero and

one nodal diameter were assigned a modal damping ratio, ζ, using the approximate values proposed by Thompson [33]:

$$\zeta = \begin{cases} 10^{-2} & \text{for} \quad n = 1 \\ 10^{-3} & \text{for} \quad n = 0 \end{cases} \tag{12}$$

Table 2. Measured eigenfrequencies and damping ratios for Wheel type A in [21]

Mode (n,0)		**2,0**	**3,0**	**4,0**	**5,0**	**6,0**	**7,0**	**8,0**
Measured frequency	Hz	387.0	972.5	1759.4	2649.0	3591.8	4547.5	5482.9
Frequency (FEA model)	Hz	383.6	954.8	1728.0	2602.4	3527.2	4469.4	5404.0
Damping ratio ($\times 10^{-4}$)		2.6	0.9	2.2	0.9	0.6	0.6	0.9
Mode (n,R)		**2,R**	**3,R**	**4,R**	**5,R**	**6,R**	**7,R**	**8,R**
Measured frequency	Hz	1671.1	2113.9	2624.7	3232.4	3936.5	4736.0	5639.4
Frequency (FEA model)	Hz	1707.9	2129.1	2630.9	3224.6	3912.0	4689.8	5553.0
Damping ratio ($\times 10^{-4}$)		2.3	0.9	0.9	0.8	0.8	0.6	0.6
Mode (n,1)		**2,1**	**3,1**	**4,1**	**5,1**	**6,1**		
Measured frequency	Hz	2223.7	2984.7	3816.0	4666.9	5396.3		
Frequency (FEA model)	Hz	2297.0	2946.1	3690.6	4468.5	5263.0		
Damping ratio ($\times 10^{-4}$)		3.4	1.6	0.8	1.4	2.2		
Mode (n,2)		**2,2**	**3,2**	**4,2**				
Measured frequency	Hz	4856.3	5416.3	6032.7				
Frequency (FEA model)	Hz	4882.2	4947.3	5473.8				
Damping ratio ($\times 10^{-4}$)		1.7	6.0	0.7				
Mode (n,C)		**0,C**	**2,C**					
Measured frequency	Hz	111.3	4240.4					
Frequency (FEA model)	Hz	730.4	4189.6					
Damping ratio ($\times 10^{-4}$)		15.2	1.2					

In addition the (1,R) mode was assigned a damping ratio of 1 since this mode appears too strongly in the frequency response function (FRF) when the influence of the axle is disregarded [33]. The (0,C) mode that was previously found by Huang et al. [9] as the unstable mode in the presence of falling friction was included in the model by using the modeshape amplitude and damping ratio determined from a single degree of freedom curve fit of the (0,C) mode in the experimentally obtained point circumferential receptance. In addition the (0,0) mode was assigned a frequency of 231 Hz to correspond with the first peak in the point radial FRF.

The vertical and longitudinal contact point mobilities and the vertical/longitudinal cross contact point mobility for a point on the wheel tread 105 mm from the back of flange, were calculated using modal summation including the effects of wheel rotation. See Figure 6. This was done using a frequency resolution of 0.1 Hz and a vehicle speed of 60 km/h. The mobilities were calculated using the eigenmodes and eigenfrequencies calculated from the FE model.

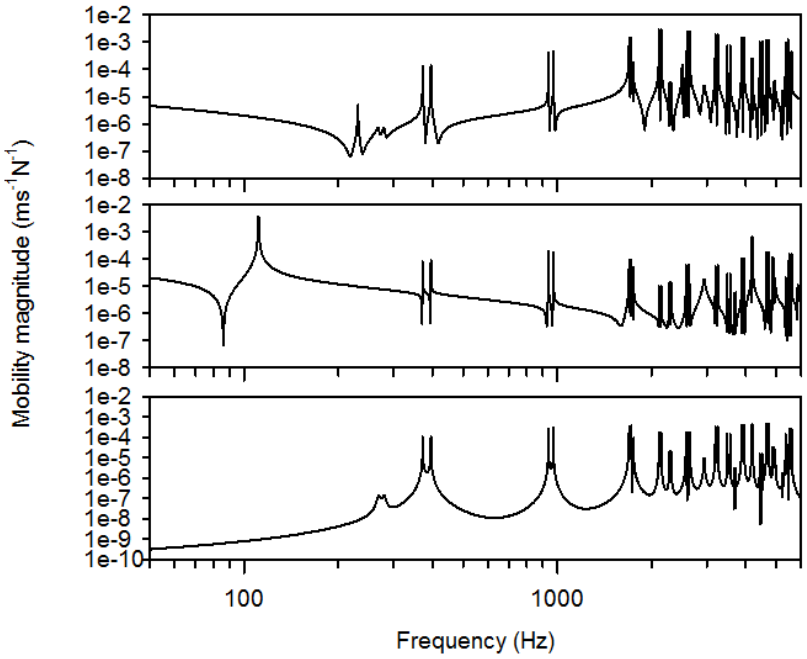

Figure 6. Contact point mobilities of wheel including the effects of wheel rotation (moving load)

4.3 Rail model

The vertical dynamics of the track is represented by a Timoshenko beam resting on a continuous two-layer elastic foundation [33]. Damping of the rail, rail pads and ballast were modelled using hysteretic damping based on a constant loss factor.

The Timoshenko beam model assumed the cross sectional properties of an UIC60 rail. The vertical rail pad stiffness per unit length was 150 MN/m^2, corresponding to a soft rail pad, whilst the vertical ballast stiffness per unit length was 100 MN/m^2. The damping loss factors of the rail pad, ballast and the rail were 0.2, 1.0 and 0.02 respectively. The damping loss factor of the rail was chosen as 0.02 to model the increase in damping of the rail pad at higher frequencies and associated with large motion of the rail foot [33]. The sleepers were assigned a mass per unit length of 230 kg/m. The rail material data used in the model was a Modulus of Elasticity of 210 GPa, a Shear Modulus of 79 GPa and a density of 7850 kg/m^3.

The longitudinal dynamics of the track is modelled as a uniform infinite bar in flexural extension resting on a continuous support [40]. The longitudinal rail pad stiffness per unit length was 75 MN/m^2, corresponding to a soft rail pad, whilst the longitudinal ballast stiffness per unit length was 50 MN/m^2. Damping of the rail pads and ballast were assigned a viscous damping coefficient per unit length of 60 kNs/m^2 and 80 kNs/m^2 respectively. The uniform infinite bar also assumed the cross sectional properties of an UIC60 rail and the rail material data as listed above for the vertical dynamics model.

The vertical/longitudinal cross-coupling dynamics of the rail in the wheel-rail contact point is not considered in the current study, i.e. $Y_{r,31} = 0$.

4.4 Contact spring

In the contact zone, only the vertical and longitudinal-tangential contact springs are considered. The equivalent Hertzian contact spring stiffness, K_H, was calculated for the known lateral contact displacements of a number of known squealing wheel profiles in combination with the measured rail profiles of the test curve using the kinematic simulation software RsGeo [41].

In the test curve, squeal only occurred for wheels under empty iron ore wagons, having a design wheel load of 25 kN. A distribution graph of the vertical load reacted by the trailing inner wheels in contact with the low rail for 2394 empty ore wagons in the 1000 m radius test curve is shown in Figure 7. Here the minimum recorded wheel load at the trailing inner wheel contact of the measured bogies was 11.92 kN and the maximum 29.74 kN. These measurements were recorded during the field tests presented in [21]. Trailing inner wheels that squealed recorded wheel loads between 13 kN and 24 kN. Using the simulation software RsGeo, this yielded a range for the normal contact spring stiffness considered in the model between 6×10^8 N/m (13 kN) and 8×10^8 N/m (24 kN).

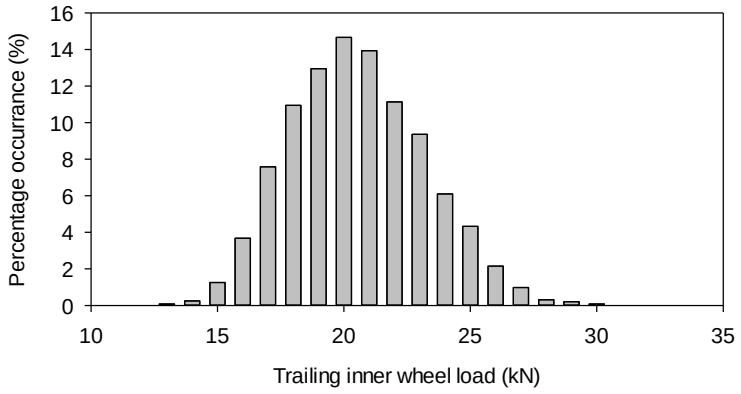

Figure 7. Trailing inner wheel, wheel load distribution

The contact between two elastic bodies has stiffness in the longitudinal-tangential direction, K_{L1}, given by [33]

$$K_{L1} = K_H \left[1 + \frac{\nu}{1-\nu}\left(\frac{1}{4} + \frac{1}{\pi}\tan^{-1}\frac{a}{b}\right)\right] \tag{13}$$

where ν is the Poisson's ratio and a and b the contact area half axes of the assumed elliptical contact area in the longitudinal and transverse directions.

For the contact parameters defined in Table 1 and a Poisson's ratio of 0.3

$$K_{L1} = 1.25K_H \tag{14}$$

The vertical/longitudinal cross-coupling dynamics of the contact area is not considered in the current model, i.e. $Y_{c,31} = 0$.

5 Results

This section provides the results of the model in terms of the potential unstable frequencies predicted by the model for a contact position 105 mm from the back of flange. It also contains a qualitative comparison of the model against on-track measurements.

5.1 On-track measured squeal frequencies

Figure 8 shows the spread of measured squeal frequencies against wheel diameter for the modelled wheel type (wheel type A in [21]) as measured in the 1000 m radius test curve. The squeal frequencies have previously been related to the (2,C), (6,R) and (7,R) modes of the wheel [21]. Because three wheel types from different manufacturers are used on the studied railway line, it was necessary to correlate each squeal frequency with one of the three wheel types. This was done by identifying the wheel type of each squealing wheel (identified during the measurement campaign) from a slow speed video recording of trains leaving the departure yard. All

squealing events recorded during the measurement campaign in [21] could be uniquely attributed to the curve-inner wheel of the trailing axle of the two-axle Scheffel bogies. During this investigation the unique wagon, its travelling direction (forward or reverse) and bogie number was identified from the vehicle identification tags mounted on the wagons. Because the same wheel type can have in-service diameters between 870 mm and 916 mm it was necessary to obtain the wheel diameter of each squealing wheel from the wheel profile monitoring system located on the railway line to correlate the squeal frequency with a wheel diameter. By relating the squeal frequency and wheel diameter data, the squeal frequency data for each wheel type changed from being "chaotic" to being ordered and usable. After this relationship was obtained between the squeal frequency and wheel diameter it was possible to correlate each set of linear varying data with a unique natural frequency of the wheel through experimental modal analyses. Modal analysis was only conducted for a wheel with maximum diameter, i.e. 916 mm, as the linear relationship between squeal frequency and diameter made it possible to study the modal behaviour of any wheel with known diameter and not necessarily the identified squealing wheels underneath the CR13/14 Iron Ore wagons.

It is evident from Figure 8 that squeal for the modelled wheel is predominantly associated with the (2,C) mode, with very few occurrences due to the (6,R) and (7,R) modes. The experimentally determined vertical and longitudinal point receptances for a 916 mm diameter wheel for a point on the wheel tread 105 mm from the back of flange are shown in Figure 9. In addition Figure 9 shows the squeal frequencies estimated from the linear regression lines in Figure 8 for a 916 mm diameter wheel as the black arrows in Figure 9.

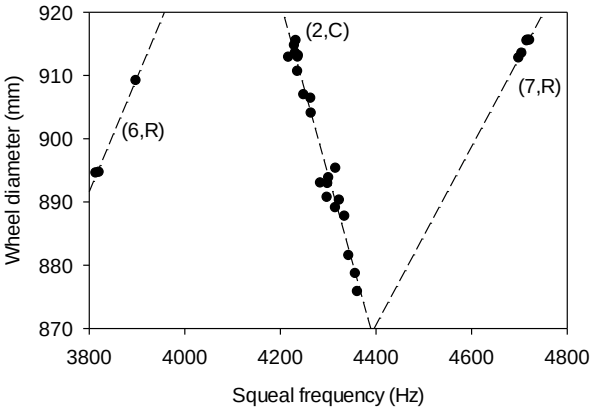

Figure 8. Measured squeal frequencies for modelled wheel (Redrawn from [21])

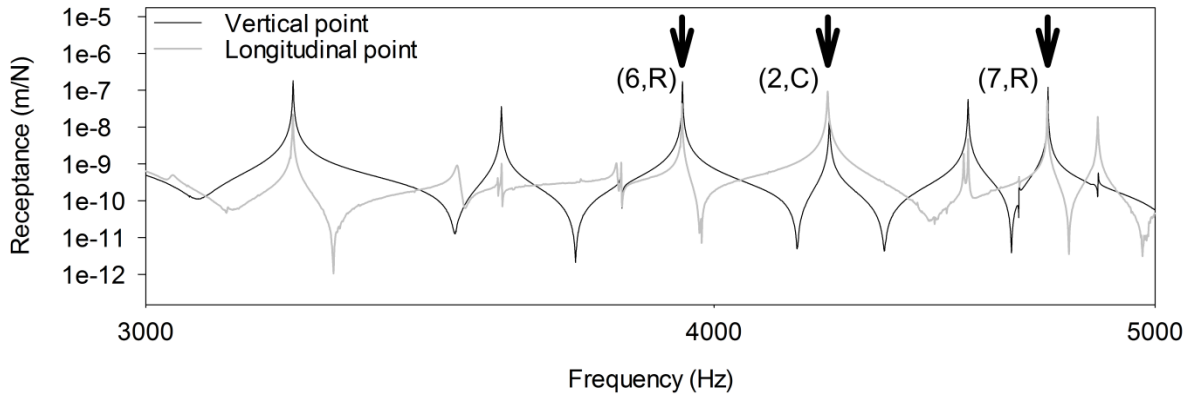

Figure 9. Magnitude of wheel receptances (vertical point and longitudinal point) on wheel tread measured for a 916 mm diameter wheel in relation to squeal frequencies (Redrawn from [21])

5.2 Model results: $k_H = 8 \times 10^8$ N/m

Figure 10 shows a stability chart for the modelled wheel for a position 105 mm from the back of the flange. For this stability chart the Hertzian contact spring stiffness was selected as 8×10^8 N/m, corresponding to the upper range of wheel loads recorded for the squealing wheels, i.e. 24 kN.

The stability chart shows the assumed adhesion curve, in addition to the loop gain exceeding one (indicating instability) for all the potential unstable frequencies found in the model as a function of longitudinal creepage. It is evident from the stability chart that two regions can be identified where different wheel modes have the largest loop gain for the range of longitudinal creepage associated with that region on the stability chart. For the region with longitudinal creepage between 0.55 % and 0.64 %, the (2,C) doublet mode pair has the largest loop gain and will be unstable, whereas for creepage values exceeding 0.64 % the (0,C) mode has the largest loop gain and will be unstable. From the stability chart it is evident that the instability associated with the (2,C) doublets occur for the region on the adhesion curve in close proximity to the adhesion optimum. The adhesion optimum is indicated with the vertical dotted line in Figure 10.

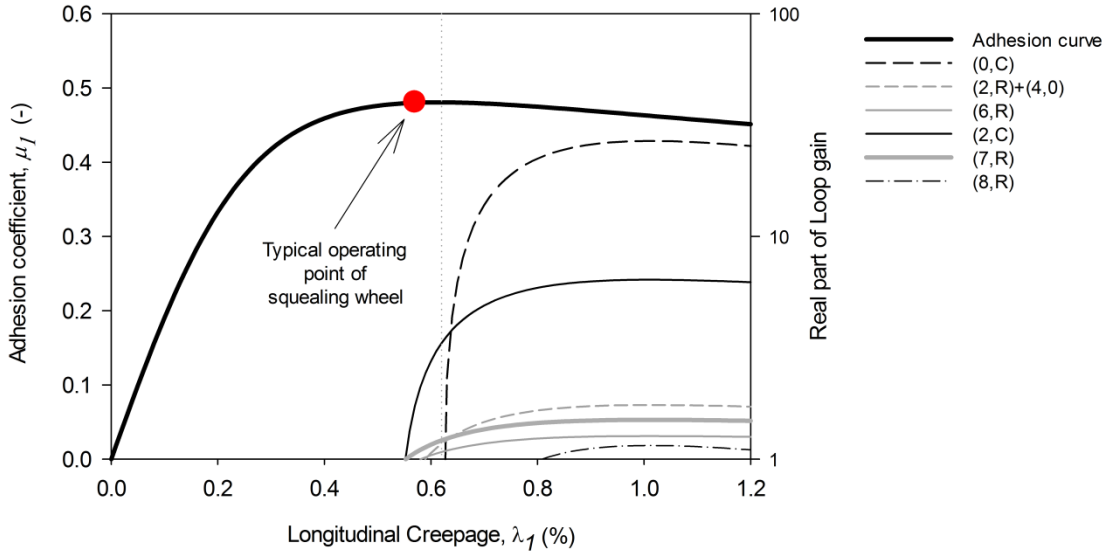

Figure 10. Stability chart for a contact position 105 mm from back of flange ($k_H = 8 \times 10^8$ N/m)

To understand the relative importance of mode-coupling and falling friction to the instabilities calculated beyond the adhesion optimum it is necessary to evaluate the individual contributions of the terms $-Y_{11}\frac{F_3}{V}\frac{\partial \mu_1}{\partial \lambda_1}$, $\frac{Y_{13}Y_{31}}{Y_{33}}\frac{F_3}{V}\frac{\partial \mu_1}{\partial \lambda_1}$ and $-(\mu_1)\frac{Y_{31}}{Y_{33}}$ in Eq. (11) to the loop gain plotted in Figure 9. These terms will be referenced as Terms 1 to 3 in the rest of the paper. Terms 1 and 2 represent excitation due to falling friction as a consequence of the longitudinal dynamics and the longitudinal/vertical cross-coupling dynamics respectively. Term 3 represents the influence of variations in the normal force on the lateral force and indicative of mode-coupling instability.

Below the adhesion optimum, the gradient of the adhesion curve is positive and provides positive frictional damping in Terms 1 and 2. Modes excited due to falling friction in term 1 (due to longitudinal dynamics) will be inherently stable for values of longitudinal creepage below the adhesion optimum. Because both Terms 1 and 2 contain the term $\frac{Y_{31}}{Y_{33}}$ it is anticipated that modes unstable due to mode-coupling will be influenced by both negative and positive frictional damping.

The relative contribution to the loop gain associated with mode-coupling and falling friction is quantified for the point on the adhesion curve with the maximum negative gradient. This corresponds to a longitudinal creepage of 1.01 % with a gradient of -6.1. Only the frequency range between 4170 Hz and 4210 Hz is considered, containing the forward and backward travelling waves associated with the (2,C) doublet modes The result of this exercise is plotted in Figures 11(a) to (e) as a Bode plot of the open loop transfer function for the frequency range between 4170 Hz and 4210 Hz. Figure 11(a) corresponds to Term 1, Figure 11(b) to Term 2, Figure 11(c) to the sum of Terms 1 and 2, Figure 11(d) to Term 3 and Figure 11(e) to the sum of Terms 1, 2 and 3. Figure 11(a) shows that the wheel-rail contact coupled system in vicinity of the (2,C) travelling waves have a positive loop gain (phase of 0°) at frequencies of 4178.1 Hz and 4201.1 Hz. These frequencies are associated with the resonance frequencies of the backward and forward travelling waves of the wheel associated with the (2,C) doublets. Figure 12 shows frequencies of 4178.1 Hz and 4201.1 Hz on a plot of the contact point longitudinal mobility of the wheel. Figure 10(b) indicates that the wheel-rail contact coupled system has got a positive loop gain for frequencies of 4182.2 Hz and 4207.0 Hz corresponding to an anti-resonances in Y_{33}. Figure 13 shows frequencies of 4182.2 Hz and 4207.0 Hz on a plot of the contact point radial mobility of the wheel-rail contact-coupled system. An anti-resonance in Y_{33} corresponds to a peak in the normal contact force spectrum and a resonance of the contact-coupled system [33]. Figure 11(b) further shows that the system has a negative loop gain (phase of 180°), i.e. taking energy out of the system, at 4178.1 Hz and 4201.1 Hz. This counteracts the loop gain associated with the longitudinal wheel dynamics and leaves the system stable for the backward and forward (2,C) travelling waves associated with the forward and backward travelling waves of the wheel. See Figure 10(c). Figure 11(c) further shows that only the resonances associated with the contact-coupled system will be unstable for the (2,C) doublets due to falling friction. Figure 11(d) indicates the wheel-rail contact coupled system (for positive creepage) is unstable at 4182.2 Hz (phase of 0°) and acts as a dynamic absorber at 4207 Hz (phase of 180°). By combing all three terms, Figure 11(e) shows that the system, for positive creepage, is only unstable in the contact-coupled resonance associated with the backward travelling (2,C) wave. Here the instability has almost equal contributions due to falling friction and mode-coupling. For negative creepage the system will be unstable in the contact-coupled resonance associated with the forward travelling (2,C) wave.

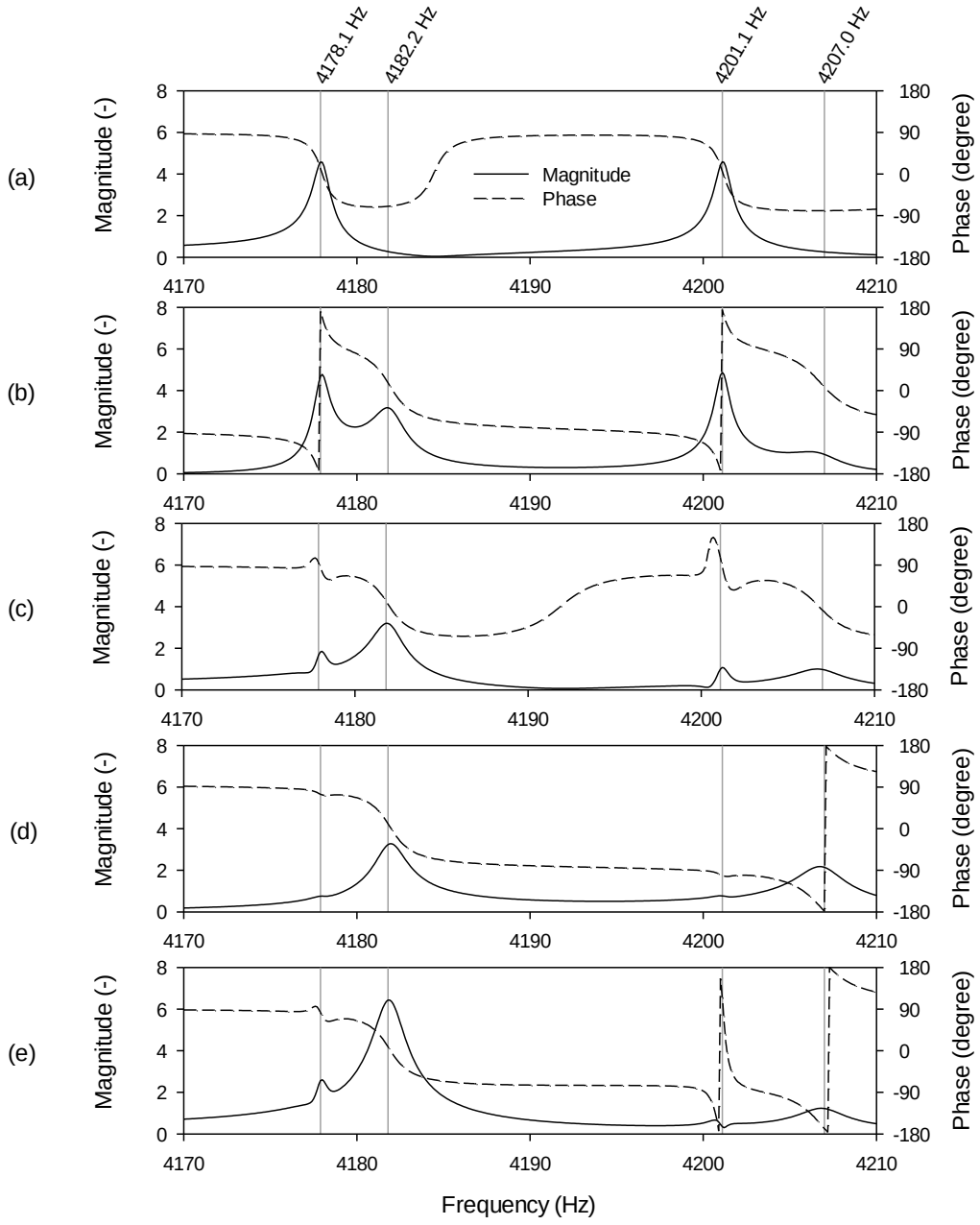

Figure 11. Bode plot of open loop transfer function: (a) Term 1 – falling friction associated with longitudinal dynamics, (b) Term 2 – falling friction associated with longitudinal/vertical cross-coupling dynamics, (c) Sum of Terms 1 and 2, (d) Term 3 – Mode-coupling, (e) Sum of Terms 1, 2 and 3.

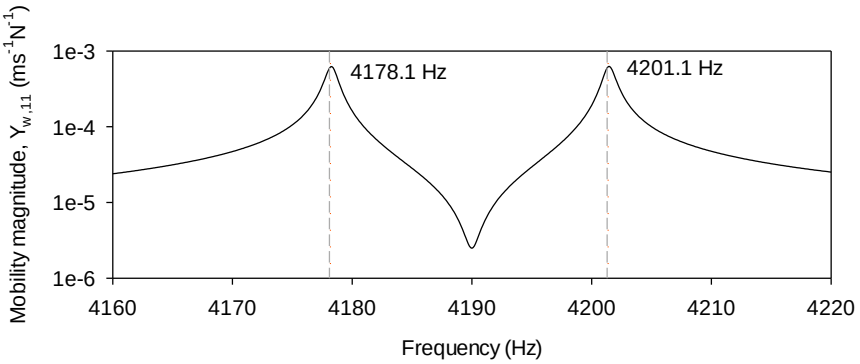

Figure 12. Mobility magnitude of $Y_{w,11}$ showing 4178.1 Hz and 4201.1 Hz

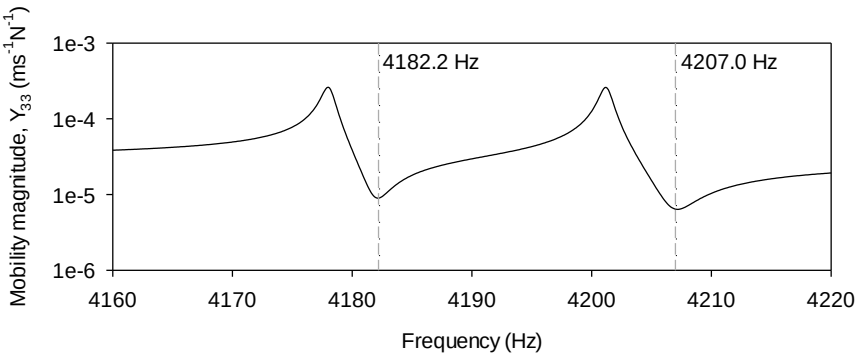

Figure 13. Mobility magnitude of Y_{33} showing 4182.2 Hz and 4207 Hz

Based on the above it can be concluded (i) that for creepages below the adhesion optimum modes are unstable due to mode-coupling and influenced by positive frictional damping and (ii) that for creepages beyond the adhesion optimum modes are unstable due to either falling friction alone (e.g. (0,C) mode) or due a combination of mode-coupling and falling friction (e.g. (2,C) doublets).

Figure 14 shows the gradient of the adhesion curve as a function of longitudinal creepage and also shows the two regions of instability where mode-coupling and falling friction are responsible for the instability. Instability of the (2,C) doublets simulated for wheels curving with longitudinal creepage close to the adhesion optimum, correlates with the wheel mode that was found predominantly unstable during infield squeal measurements as shown in Figure 8. Instability due to the (6,R) and (7,R) doublet modes that were also found during the infield tests will likely not be excited in squeal for the wheel-rail contact conditions depicted in Figure 10, i.e. although they are predicted as potentially unstable modes they never have the largest loop gain for any range of longitudinal creepage. Instability due to the (0,C) mode occurring at 111.3 Hz is not relevant to squeal and will instead cause rail corrugation or wheel polygonisation.

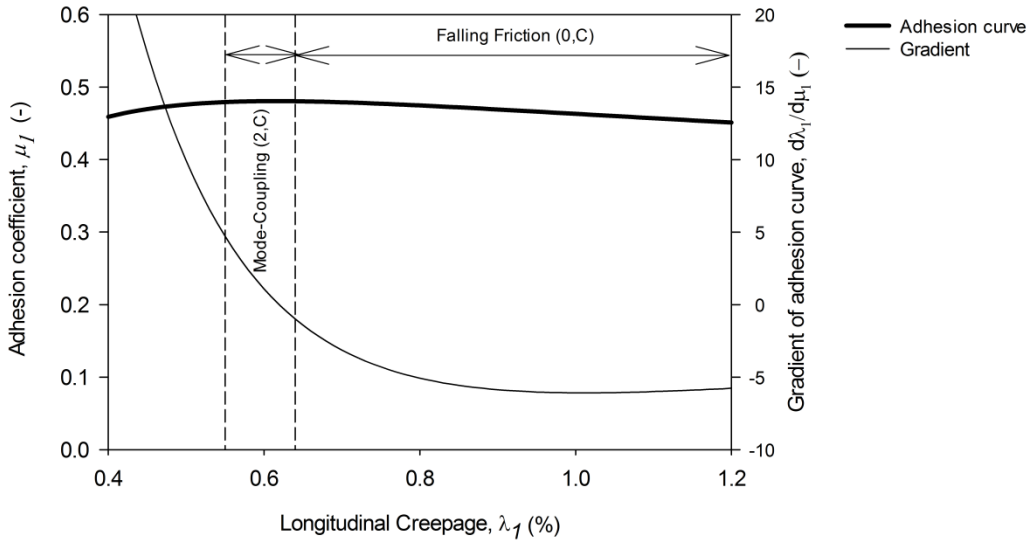

Figure 14. Instability regions as a function of the gradient of the adhesion curve

5.3 Model results: $k_H = 6 \times 10^8$ N/m

Figure 15 shows a stability chart for the modelled wheel for a position 105 mm from the back of flange. For this stability chart the Hertzian contact spring stiffness was selected as 6×10^8 N/m, corresponding to the lower range of wheel loads recorded for the squealing wheels, i.e. 13 kN.

The stability chart in Figure 15 shows that three regions can be identified where different wheel modes have the largest loop gain for a given range of longitudinal creepage. In addition to the regions where the (0,C) mode and (2,C) doublet modes have the largest loop gain, the third region predicts the (7,R) doublets with the largest loop gain for longitudinal creepages between 0.53 % and 0.57 %. The fact the current model only predicts squeal associated with the (7,R) doublets for a small range of creepages and for wheel's having significant quasi-static wheel unloading might start explaining the infield observations according to Figure 7 that the (7,R) doublets does not squeal very often in the test curve.

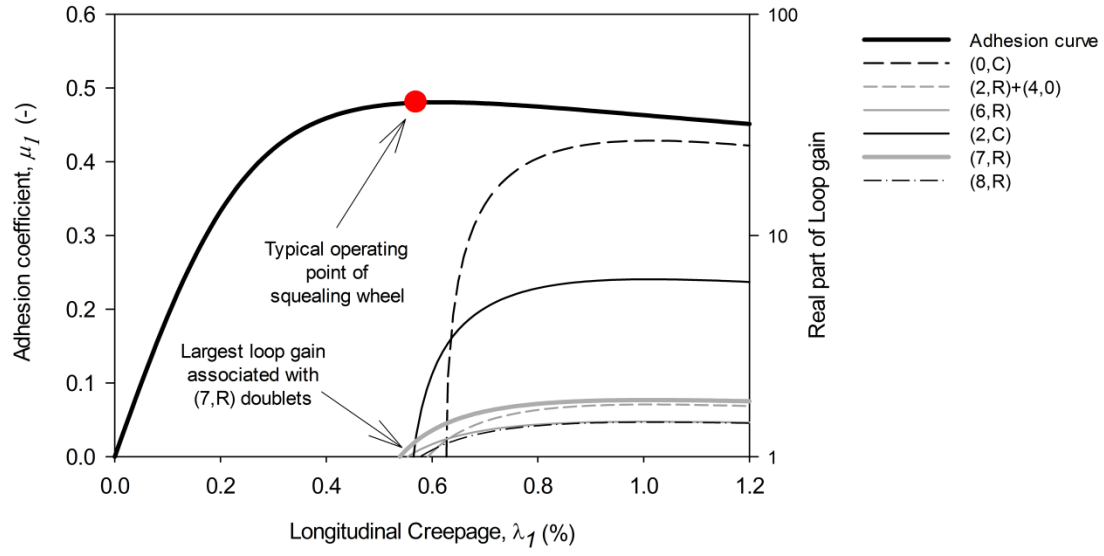

Figure 15. Stability chart for a contact position 105 mm from back of flange ($k_H = 6 \times 10^8$ N/m)

Changing the Hertzian contact stiffness changes the magnitude of anti-resonances in Y_{33}, which has a direct impact on the calculated loop gain for the mode coupling term $-\mu Y_{31}/Y_{33}$. Figure 16 compares the mobility magnitude for Y_{33} calculated with a normal contact spring stiffness of 8×10^8 N/m and 6×10^8 N/m respectively. The anti-resonances that are associated with instability due to the (2,C) and (7,R) backward travelling waves are additionally encircled in Figure 15. The magnitude shift of the anti-resonances changes the loop gain for constant friction by influencing the term $-\mu Y_{31}/Y_{33}$, as well as the rate of change of the loop gain due to the influence of frictional damping by influencing the term $\frac{Y_{13}Y_{31}}{Y_{33}}\frac{F_3}{V}\frac{\partial \mu_1}{\partial \lambda_1}$. This interplay between the loop gain for constant friction and the rate of change of the loop gain due to a magnitude shift of the anti-resonances of Y_{33} plays a crucial role in selecting the squealing frequency.

The third infield squeal frequency associated with the (6,R) doublets has not been predicted as an unstable mode with the largest loop gain for any set of operational conditions simulated. Instead it is postulated that a change in wheel diameter might result in the model predicting the (6,R) doublets as unstable instead of the (7,R) doublets. This is based on the experimental deduction in Figure 8 that squeal associated with the (6,R) doublets only occurred for wheels with a diameter between 894 mm and 909 mm, whereas squeal associated with the (7,R) doublets occurred for wheels with a diameter between 913 mm and 916 mm which is similar to the modelled wheel diameter of 916 mm.

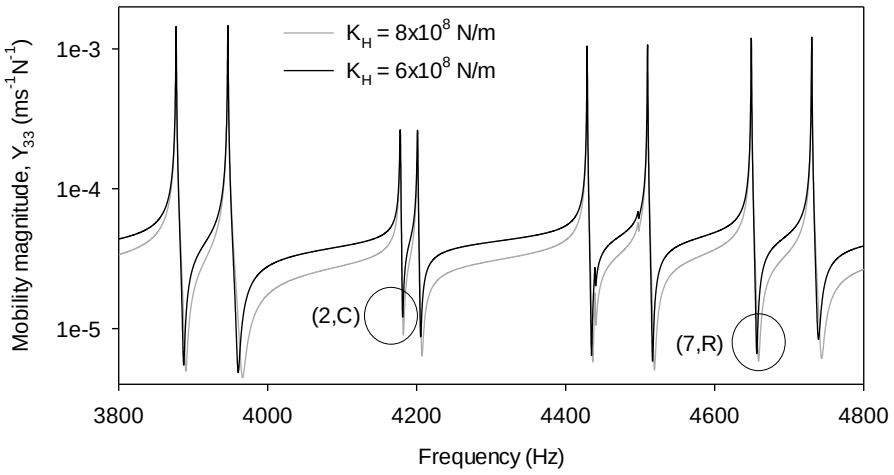

Figure 16. Mobility magnitude (Y_{33}) for different Hertzian contact stiffnesses

6 Instability mechanism

From [7], the dynamic normal force in the wheel-rail contact is related to the dynamic longitudinal force. This term can be interpreted as the magnitude and phase relationship between a normal and tangential dynamic force that will give identical vibrational responses in the wheel-rail contact. The relationship for positive creepage being

$$f_3 = -\frac{Y_{31}}{Y_{33}} f_1 \tag{15}$$

The term $-Y_{31}/Y_{33}$ can also be found in Eq. (11) describing the loop gain for the dynamic longitudinal-tangential force. For a case with constant friction Eq. (11) simplifies to

$$-(\mu_1)\frac{Y_{31}}{Y_{33}} \tag{16}$$

It is enough to consider a case with constant friction, because the described instability mechanism most likely occurs for a point close to the adhesion optimum where falling friction doesn't contribute to the instability.

Figure 17 shows a Bode plot of the transfer function $-Y_{31}/Y_{33}$ in the vicinity of the backward and forward travelling waves associated with the (2,C) doublet mode pair. At the unstable frequency of 4182.2 Hz, associated with positive creepage, the transfer function reaches a local maximum with a phase of 0°. From Eq. (15) a phase of 0° means that $-Y_{31}$ and Y_{33} (or $-\alpha_{31}$ and α_{33}) has got the same phase at 4182.2 Hz. The fact that $-Y_{31}$ and Y_{33} (or $-\alpha_{31}$ and α_{33}) has got the same phase at 4182.2 Hz is again illustrated in Figure 18 showing Bode plots of $-\alpha_{31}$ and α_{33}. The phase of both $-\alpha_{31}$ and α_{33} being $-90°$ at 4182.2 Hz.

Considering the non-symmetric friction coupling that exist between the normal force and the longitudinal-tangential friction force during sliding i.e. $f_1 = \mu_1 f_3$, a 0° phase difference exists between the dynamic friction and normal forces. Because of this 0° difference that exist between the dynamic normal and friction forces as well the fact that the vertical and vertical/longitudinal receptances (in this case the negative of the vertical/longitudinal receptance to correspond with positive creepage in Figure 3(b)) has got the same phase, an explanation for the instability is at hand. A dynamic out-of-plane displacement leads to a time varying normal force, which in return leads to a time varying friction force that is in-phase with the time varying normal force. In return the time varying friction force leads again to an out-of-plane displacement that is in-phase with the original out-of-plane displacement that caused the time varying friction force. This general description for the instability mechanism can be made specific for the instability simulated at 4182.2 Hz. The $-90°$ phase of α_{33} implies that a dynamic normal force generated by a normal displacement at 4282.2 Hz will be 90° ahead of this normal displacement. Because a 0° phase relationship exists between the dynamic normal and friction forces, the friction force will also be 90° ahead of the normal displacement. The $-90°$ phase of $-\alpha_{31}$ at 4182.2 Hz implies that a normal displacement generated by the frictional force will lag 90° behind the friction force. Because the friction force is 90° ahead of the normal displacement that resulted in the friction force, and because the normal displacement generated in return by the friction force lags the friction force by 90° the normal displacement generated by the friction force is in phase with the original normal displacement. This results in positive interference of the normal vibration at the wheel-rail contact. This cycle will continuously feed energy into the normal vibration via the friction force. With $\|\alpha_{31}\| >> \|\alpha_{33}\|$, the positive energy gain per cycle is large and vibrations can grow quickly in the presence of large longitudinal creepage. Because, the friction force also grows in magnitude during this process the longitudinal-tangential vibration at the contact will also grow until the limit cycle is reached.

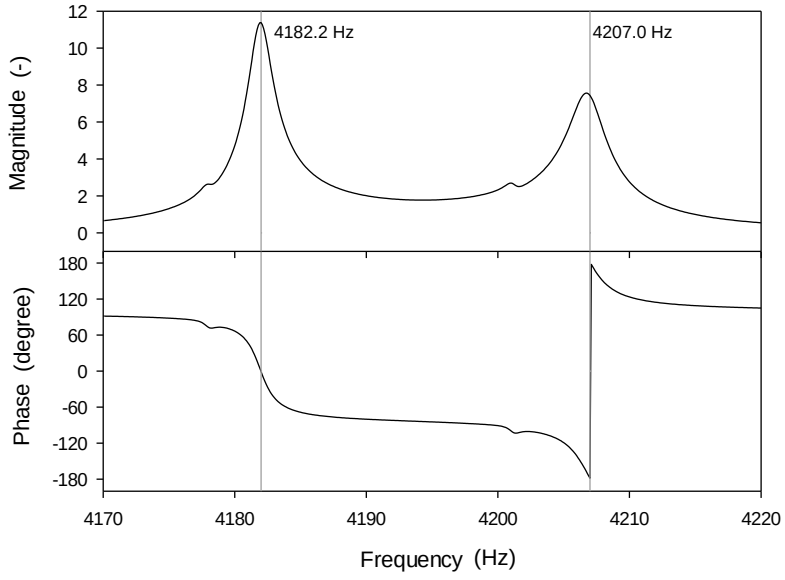

Figure 17. Bode plot of $-Y_{31}/Y_{33}$

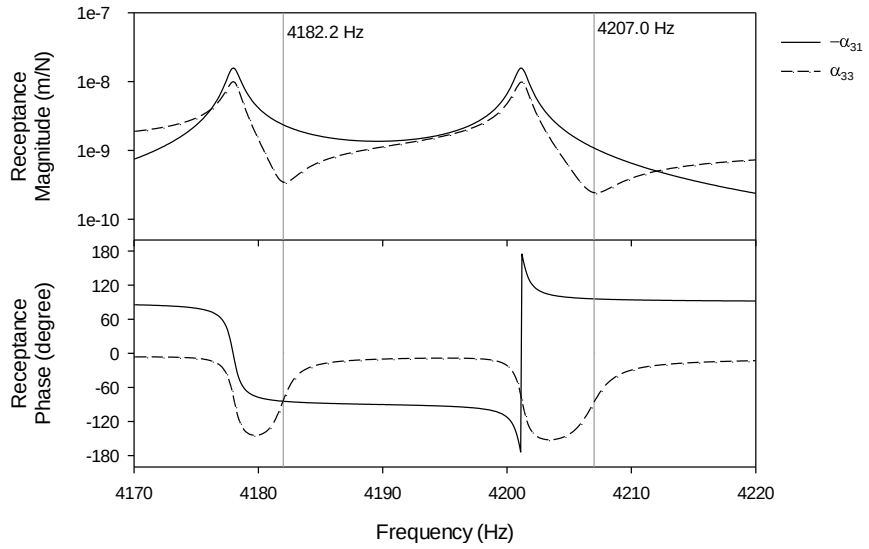

Figure 18. Bode plot of $-\alpha_{31}$ and α_{33}

At the unstable frequency of 4182.2 Hz, $f_3 = 11.4f_1$. This implies that the vertical vibration of the wheel, rail and contact spring most likely exceeds that of the same component in the longitudinal direction. Rail foot acceleration recorded during the passing of a squealing wheel during experimental measurements confirmed that the vertical rail vibration exceeds that of the longitudinal rail vibration for the identified unstable frequency. See Figure 19. The exact time that the squealing wheel passed the measurement location is indicated with a black arrow in the figure.

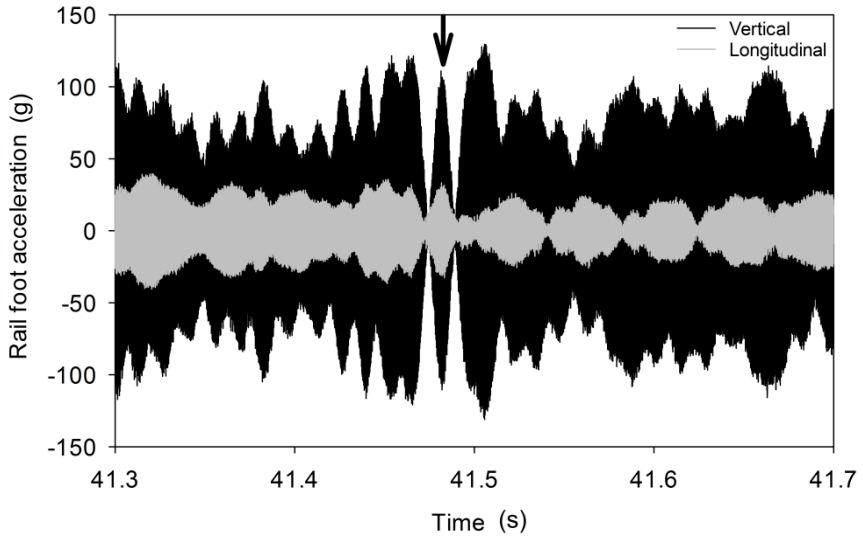

Figure 19. Rail foot acceleration during inner wheel squeal event

7 Inclusion of lateral creepage

The case of squeal studied up to this point presented in-field where the longitudinal creepage in the wheel-rail contact was exceptionally high. Vehicle dynamics simulations showed that the resulting creep force, F_r, was acting in a direction, φ, 186.3° with respect to the vehicle running direction [23].

To understand the importance of the coupling of doublet modes to the more general case of squeal due to unsteady lateral creepage it is necessary to extent Eq. (11) to include both longitudinal and lateral creepage, i.e.

$$-\left(Y_{rr}-\frac{Y_{r3}Y_{3r}}{Y_{33}}\right)\left(\frac{F_3}{V}\frac{\partial\mu_r}{\partial\lambda_r}\right)-(\mu_r)\frac{Y_{3r}}{Y_{33}} \tag{17}$$

Here the subscript r indicates the resultant direction, φ, of the creep force, F_r, with respect to the vehicle running direction as shown in Figure 20.

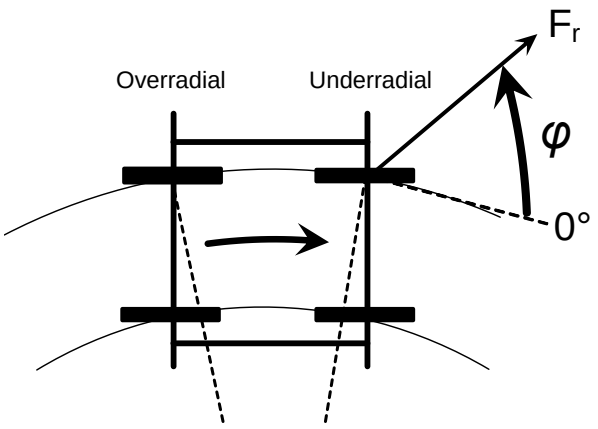

Figure 20. Definition of acting direction of resultant creep force with respect to vehicle running direction

Only a case with constant friction is considered as the described instability mechanism due to for instance the (2,C) doublets occurs for the region close to the adhesion optimum where falling friction is not important. Eq. (17) reduces to

$$-(\mu_r)\frac{Y_{3r}}{Y_{33}} \tag{18}$$

Both a case with a non-rotating sliding wheel as well as a case considering the moving load nature of a rotating wheel is considered. This allows comparing the current state-of-the-art with the case where the moving load nature of the rotating wheel is crucial to model instability in the presence of longitudinal creepage.

The onset of instability is investigated for varying friction level and direction of the resulting creep force as shown in Figure 21. Figure 21 plots the mode with the largest loop gain calculated for each combination of friction level and direction of the resulting creep force. 90° implies that the wheel is curving with an underradial (positive angle-of-attack of wheelset with curve-outer wheel attacking the high rail) curving position without longitudinal creepage and 270° implies that the wheelset is curving with an overradial (negative angle-of-attack of wheelset with curve-inner wheel attacking the low rail) position without longitudinal creepage.

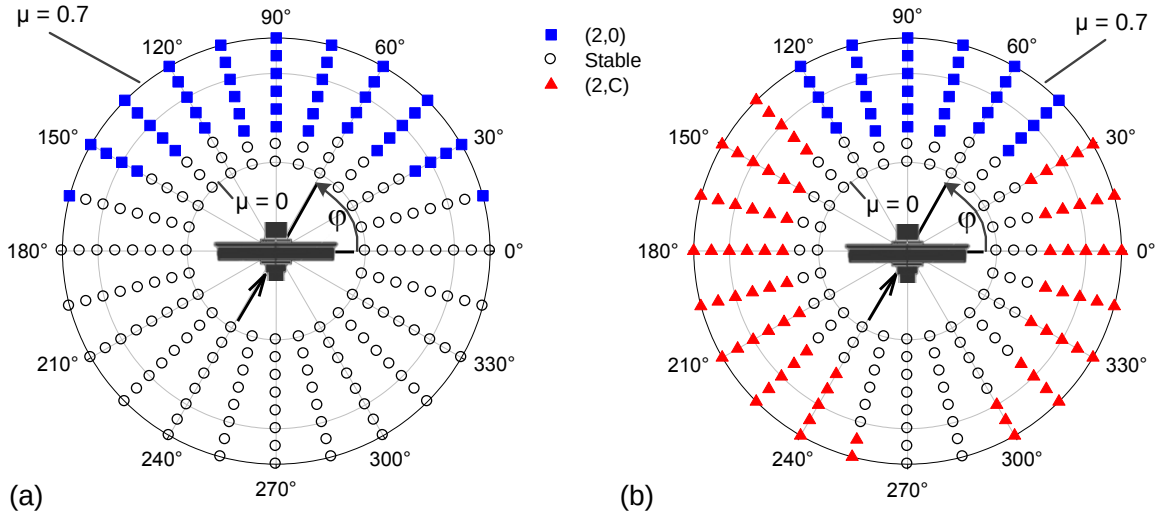

Figure 21. Largest loop gain calculated for varying directions of the resulting creep force (acting in angle φ with respect to vehicle running direction) and a wheel-rail friction coefficient in the range between 0 and 0.7. (a) Model based on non-rotating sliding wheel. (b) Model including moving load nature of rotating wheel.

Evident from Figure 21(a) for the case considering a non-rotating wheel is that instability is predicted for an underradial curving position, whilst no instability is predicted for the wheel curving in an overradial curving position or for the resulting creep force acting in a pure longitudinal direction ($\varphi = 0°$ or $\varphi = 180°$). These results are similar to those presented in [13]. For the case considering the moving load nature of a rotating wheel, Figure 21(b) shows how the contact coupled system can be unstable for almost any direction of the resulting creep force, except when the wheel curves with an overradial curving position without longitudinal creepage. Here depending on the direction of the creep force a wheel curving with negligible spin creepage (i.e. a small contact angle) can squeal in either its (2,0) or (2,C) modes depending on the direction of the resultant creep force and friction level.

8 Conclusion

Railway wheel squeal with longitudinal creepage as the source of instability was modelled. In contrast to international research that does not consider longitudinal creepage to be relevant to squeal, the results of this research demonstrate the importance of longitudinal creepage as a source of instability for squeal. The research further showed that modelling the dynamics of a wheel including the effects of a rotating wheel under moving load excitation is crucial to understanding the instability. This captures the cross-coupling dynamics between the normal and longitudinal degrees-of-freedom (with respect to the contact patch) that is otherwise zero for a stationary wheel.

Both instability due to falling friction and mode-coupling were assessed. The results of the model show that the excitation of squeal due to mode-coupling is limited to the region on the adhesion curve close to adhesion optimum where the positive and negative frictional damping is very small. For the simulated wheel the resonances of the contact coupled wheel-rail system associated with the backward travelling waves of the (2,C) and (7,R) doublets could be shown to participate in squeal. In this case the operational conditions associated with longitudinal creepage and the wheel load could be shown to take part in determining which of the potentially unstable modes will have the largest loop gain and will be excited into squeal. For the falling region of the adhesion curve, beyond a certain gradient the fundamental torsional resonance of the wheelset will be unstable. Because of the low frequency of the (0,C) mode, the predicted instability is not relevant to squeal and instead relevant to the formation of rail corrugation and wheel polygonisation.

The results of the model based on unsteady longitudinal creepage provide good agreement with experimental findings in terms of the experimentally obtained squeal frequencies as well as being able to predict the dominant squeal mode in the test curve as the mode with the largest loop gain for most operational conditions i.e. the (2,C) mode.

Extending the model based on unsteady longitudinal creepage to include lateral creepage shows that the wheel-rail vibration can be dominated by the (2,C) doublets for the resulting creep force acting in directions between 0° and 30°, between 135° and 255° as well as between 300° and 360°.

Positive flow of energy for the modelled case of squeal results from the dynamic friction and normal forces at the unstable frequency being in phase with one another as well as the friction force causing normal displacement at the wheel-rail contact that is in phase with the normal displacement that caused the normal force in the first place. This closed phase loop causes positive interference of the normal vibration in the wheel-rail contact and allows the vibration amplitude to grow. Although this mechanism is different from that shown by Hoffmann et al. [24] for a general case with mode-coupling, the non-symmetry of the stiffness matrix associated with friction is still the root cause leading to instability in the presented case of squeal.

Based on the results presented in this paper, more attention should be paid to the effect of longitudinal creepage and wheel rotation in the modelling of squeal going forward.

References

1. Rudd MJ. Wheel/rail noise – Part II: Wheel squeal. Journal of Sound and Vibration 1976; 46.3: 381-394.
2. Fingberg U. A model of wheel-rail squealing noise. Journal of Sound and Vibration 1990; 143.3: 365-377.
3. Périard FJ. Wheel-rail noise generation: Curve squealing by trams. PhD Thesis, Delft University of Technology, Netherlands, 1998.
4. Heckl MA and Abrahams ID. Curve squeal of train wheels, Part 1: Mathematical model for its generation. Journal of Sound and Vibration 2000; 229: 695-707.
5. De Beer FG, Janssens MHA, Kooijman PP and Vliet WJ. Curve squeal of railbound vehicles (part 1): frequency domain calculation model. Proceedings of Internoise 2000, Nice, France, vol.3: 1560-1563.
6. De Beer FG, Janssens MHA and Kooijman PP. Squeal noise of rail-bound vehicles influenced by lateral contact position. Journal of Sound and Vibration 2003; 267: 497-507.
7. Thompson DJ and Monk-Steel AD. A Theoretical model for curve squeal. Report for UIC project Curve Squeal. Institute of Sound and Vibration Research, University of Southampton, UK, 23 February 2003.
8. Chiello O, Ayasse JB, Vincent N and Koch JR. Curve squealing of urban rolling stock – Part 3: Theoretical model. Journal of Sound and Vibration 2006; 293: 710-727.
9. Huang ZY, Thompson DJ and Jones CJC. Squeal prediction for a bogied vehicle in a curve. In Schulte-Werning B, et al. (eds.) Noise and Vibration Mitigation for Rail Transportation Systems. NNFM, vol. 99, pp 313-319. Springer, Heidelberg, 2008.
10. Chen GX, Xiao JB, Liu QY and Zhou ZR. Complex eigenvalue analysis of railway curve squeal. In Schulte-Werning B, et al. (eds.) Noise and Vibration Mitigation for Rail Transportation Systems. NNFM, vol. 99, pp 433-439. Springer, Heidelberg, 2008.
11. Glocker C, Cataldi-Spinola E and Leine RI. Curve squealing of trains: Measurement, modelling and simulation. Journal of Sound and Vibration 2009; 324: 695-702.
12. Pieringer A. A numerical investigation of curve squeal in the case of constant wheel/rail friction. Journal of Sound and Vibration 2014; 333: 4295-4313.
13. Pieringer A, Torstensson P, Giner J and Baeza L. Investigation of railway wheel squeal using a combination of frequency- and time-domain models. In: Proceedings of the 12th International workshop on railway noise, Terrigal, Australia, September 2017: 444-451.
14. Wang C, Dwight R, Wenxu L and Jiandong J. Prediction on curve squeal in the case of constant wheel-rail friction. In: Proceedings of the 12th International workshop on railway noise, Terrigal, Australia, September 2017: 428-433.

15. Remington PJ. Wheel-rail squeal and impact noise: What do we know? What don't we know? Where do we go from here? Journal of Sound and Vibration 1985; 116: 339-353.
16. Curley D, Anderson DC, Jiang J and Hanson D. Field trials of gauge face lubrication and top of rail friction modification for curve noise mitigation. In Nielsen JCO, et al. (eds.) Noise and vibration mitigation for rail transportation systems. NNFM 2015; 126: 449-456.
17. Jiang J, Anderson DC and Dwight R. The mechanisms of curve squeal. In Nielsen JCO, et al. (eds.) Noise and vibration mitigation for rail transportation systems. NNFM 2015; 126: 587-594.
18. Zenzerovic I, Time-domain modelling of curve squeal: a fast model for one- and two-point wheel-rail contact. PhD Thesis, Chalmers University of Technology, Gothenburg, Sweden 2017.
19. Squicciarini G, Usberti S, Barbera A, Corradi R and Thompson DJ. Curve squeal in the presence of two wheel/rail contact points. In Nielsen JCO, et al. (eds.) Noise and vibration mitigation for rail transportation systems. NNFM 2015; 126: 603-610.
20. Grassie SL and Kalousek J. Rail corrugations: Characteristics, causes and treatments. Journal of Rail and Rapid Transit 1993; 207.1: 57-68.
21. Fourie DJ, Gräbe PJ, Heyns PS and Fröhling RD. Experimental characterization of railway wheel squeal occurring in large-radius curves. Journal of Rail and Rapid Transit 2016; 230.6: 1561-1574.
22. Scheffel H. A new design approach for railway vehicle suspension. Rail International 1974; 638: 638-651.
23. Fourie DJ, Gräbe PJ, Heyns PS, Fröhling RD and Spangenberg U. New insights into curve squeal mitigation measures. In: Proceedings of the 11th International Heavy Haul Association Conference, Cape Town, South Africa, September 2017: 705-712.
24. Hoffmann N, Fischer M, Allgaier R and Gaul L. A minimal model for studying properties of the mode-coupling type instability in friction induced oscillations. Mechanics Research Communications 2002; 29: 197-205.
25. Thompson DJ. Wheel-rail noise generation, part V: Inclusion of wheel rotation. Journal of Sound and Vibration 1993; 161.3: 467-482.
26. Pieringer A, Baeza L and Kropp W. Modelling of railway curve squeal including effects of wheel rotation. In Nielsen JCO, et al. (eds.) Noise and Vibration Mitigation for Rail Transportation Systems. NNFM, Springer, Heidelberg 2015. 126: 417-424.
27. Fourie DJ, Gräbe PJ, Heyns PS and Fröhling RD. Wheel squeal as a result of unsteady longitudinal creepage. In: Proceedings of the 12th International workshop on railway noise, Terrigal, Australia, September 2016: 36-45.
28. Kalker JJ. A Fast Algorithm for the Simplified Theory of Rolling Contact, Vehicle System Dynamics 1982; 11: 1-13.
29. Kalker JJ, Three-Dimensional Elastic Bodies in Rolling Contact. 1st ed. Kluwer: Dordrecht, Netherlands, 1990.
30. Vermeulen PJ and Johnson KL. Contact of nonspherical elastic bodies transmitting tangential force. Trans. ASME, Series E, Journal of Applied Mechanics 1964; 31: 338-340.
31. Kraft K. Der Einfluβ der Fahrgeschwindigkeit auf den Haftwert zwischen Rad und Schiene (The influence of travelling speed on the friction coefficient between wheel and rail). Archic für Eisenbahntechnik 1967; 22: 58-78.
32. Ding B, Squicciarini G and Thompson DJ. Effects of rail dynamics and friction characteristic on curve squeal. Journal of Physics: Conference Series 2016; 744 012146.
33. Thompson DJ. Railway noise and vibration: mechanisms, modelling and means of control. 1st ed. Oxford: Elsevier, 2009.
34. Polach O. Creep forces in simulations of traction vehicles running on adhesion limit. Wear 2005; 258: 992-1000.
35. Meymand SZ, Keylin A and Ahmadian M. A survey of wheel-rail contact models for rail vehicles. Vehicle System Dynamics 2016, 54.3: 386-428.

36. Magel E and Liu Y. Study of friction: measurement, analysis and practical implications for the wheel-rail contact. In: Proceedings of the 8th International Conference and Wear of Rail, Wheel Systems, Firenze, Italy, 15-18 September 2009.
37. Thompson DJ, Squicciarini G and Ding B. A state-of-the-art review of curve squeal noise: phenomena, mechanisms, modelling and mitigation. In: Proceedings of the 12th International workshop on railway noise, Terrigal, Australia, September 2017: 1-27.
38. Ding B, Squicciarini G, Thompson DJ and Corradi R. An assessment of mode-coupling and falling-friction mechanisms in railway curve squeal through a simplified approach, Journal of Sound and Vibration 2018; 423: 126-140.
39. Ouyang H, Nack W, Yongbin Y and Chen F. Numerical analysis of automotive disc brake squeal: a review. International Journal of Vehicle Noise and Vibration 2005; 1.2-4: 207-231.
40. Grassie SL, Gregory RW and Johnson KL. The dynamic response of railway track to high frequency longitudinal excitation. Journal Mechanical Engineering Science 1982; 24.2: 97-102.
41. Kik W. AcRadSchiene Version 4.4: To create or approximate wheel-rail profiles. Berlin, ArgeCare, 2010.